Journal of
Composites Science

MDPI

Article

A Self-Pumping Composite Dressing Improved Hypertrophic Scar Healing with Dual Therapy and Active-Fluid Transport

Kam-Che Lui, Nuruzzaman Noor, Chi-Wai Kan and Xungai Wang *

School of Fashion and Textiles, The Hong Kong Polytechnic University, Hung Hom, Kowloon, Hong Kong, China
* Correspondence: xungai.wang@polyu.edu.hk

Abstract: Silicone gel sheeting (SGS) and pressure garment therapy (PGT) are the International Clinical Recommendations on Scar Management's (ICRSM) two principal non-invasive scar-healing procedures. This study created a new PGT-SGS composite (PGF-Biopor®AB-based) via pre-strained screen printing. The Biopor®AB hydrophobicity and nylon-hydrophilicity enabled self-pumping for PGT-SGS dual therapy and pressure-driven "warp insertions" mobility facilitates active-fluid transportation. Integrating both therapies in a single PGT-SGS composite achieved efficacy optimization, and the 3D channel structure allowed trauma-free active-fluid transport. The 3D channel topology enables smooth diffusional transport in active-fluid transport environments—and active "nylon absorbency" improved water uptake and enhanced permeability capabilities with sustainability achieved dynamic hydration. The sole use of PGF-Biopor®AB composite in empirical trials verified dual therapy with trauma-free active-fluid transport with one-month efficacy, providing a new route for dual treatment and active scar management.

Keywords: composite dressing; scar healing; pressure garment therapy; silicone gel sheeting; dual therapy; "warp insertions" mobility

check for updates

Citation: Lui, K.-C.; Noor, N.; Kan, C.-W.; Wang, X. A Self-Pumping Composite Dressing Improved Hypertrophic Scar Healing with Dual Therapy and Active-Fluid Transport. *J. Compos. Sci.* **2023**, *7*, 192. https://doi.org/10.3390/jcs7050192

Academic Editor: Francesco Tornabene

Received: 31 March 2023
Revised: 20 April 2023
Accepted: 28 April 2023
Published: 8 May 2023

Copyright: © 2023 by the authors. Licensee MDPI, Basel, Switzerland. This article is an open access article distributed under the terms and conditions of the Creative Commons Attribution (CC BY) license (https://creativecommons.org/licenses/by/4.0/).

1. Introduction

Over 100 million patients acquire scars in developed countries annually, and the scar therapeutics market (U.S.A.) generated USD 15.3 billion in 2022 (at an 8.5% annual growth to USD 29.5 billion by 2026) [1–5]. The International Clinical Recommendations on Scar Management (ICRSM) suggests using silicone gel sheeting (SGS) as a first-line strategy for 6 weeks, followed by first-line pressure garment therapy (PGT) use for 6–12 months. Stratum corneum (SC) dehydration initiates cytokines production, dermal fibroblasts synthesis, and collagen release; the excess collagen production causes abnormal scarring [6–12]. However, the single PGT or SGS alone could not fulfill the occlusive characteristics and moisture balance request from SC dehydration [13,14]. There are still challenges in combining non-invasive treatment modalities [6,7].

Based on ICRSM guidelines and the "ideal" dressing requirements, current burn dressings only cater to certain limited requirements. According to K. J. Quinn's principles of burn dressing, an "ideal" dressing should (i) protect scar tissues from bacterial infection, (ii) provide ideal gas/vapor exchange, (iii) manage excessive biofluid, and (iv) provide an ideal healing environment with painless removal [15–17]. However, the critical roles of (i) moist scar healing with "breathability", (ii) hydration with water retention, and (iii) epithelializing faster under occlusion, have not yet been entirely addressed [18,19]. Both invasive and non-invasive options aim for efficacy optimization, optimum moisture, and trauma-free dressing properties to offer shortcuts to rehabilitation across the landscape of scar management. Studies on fluid flow characteristics focus on identifying the hydrodynamic structures by shape, size, nonlinear flow characteristics, simulation for flow characteristics, geometry influence of flow characteristics and flow pattern linking to operating performance [20–24]. The design of the PGF-Biopor® AB composite in this

study allows PGT-SGS dual therapy for first-line efficacy optimization. At the same time, the structural advancement of a self-pumping 3D channel structure with "warp insertions" mobility aims for active-fluid transport and trauma-free dressing material properties. Collective results of SGS and PGT composite showed greater hydration of the scar surface and epidermis, altered extracellular matrix (ECM) remodelling, and assisted scar maturation. A PGT-SGS dual therapy composite addresses many dressing shortcomings to-date [25–27]. This study focuses on identifying the hydrodynamic structures, internal flow features and flow routes for fluid flow characteristics and their linking to pump flow performances in terms of water vapour permeability and water uptake.

Silicone Biopor®AB (Dreve Otoplastik GmbH, Unna, Germany) is not an ideal skin simulant due to the lack of mechanical stiffness, a fibrous structure, and low mechanical properties [8,9]. Pressure garment fabric (PGF), equipping a tension-sharing textile-reinforced structure, was used to complement Biopor®AB for tension shielding and pressure redistribution [8,9]. Thus, in the creation of a PGT-SGS composite (PGF-Biopor®AB), a medical silicone matrix (Biopor®AB) is reinforced with a pressure garment fabric (PGF) and turned into a PGF-SGS composite (Figure 1). Textile Janus structure design and PGF embedding in Biopor®AB layers provide hydrophobicity, while nylon-based warp insertion absorptivity exhibits hydrophilicity, fulfilling the absorbent-hydrophobic material needs and also yielding a unidirectional fluid pump for self-pumping [28–30]. In constructing mobile warp insertions as the engine of self-pumping, pre-strained biaxial tensioning first reallocated yarn spaces to allow no Biopor®AB impregnation into the warp insertions, maintaining mobility [31,32]. Gravity, mechanical pressure, or chemical forces can be the driving forces to activate the process of self-pumping [29]. When used in bandaging material, mechanical pressure as the driving force initiates warp insertion mobility—the compressive properties and capillary forces complete self-pumping.

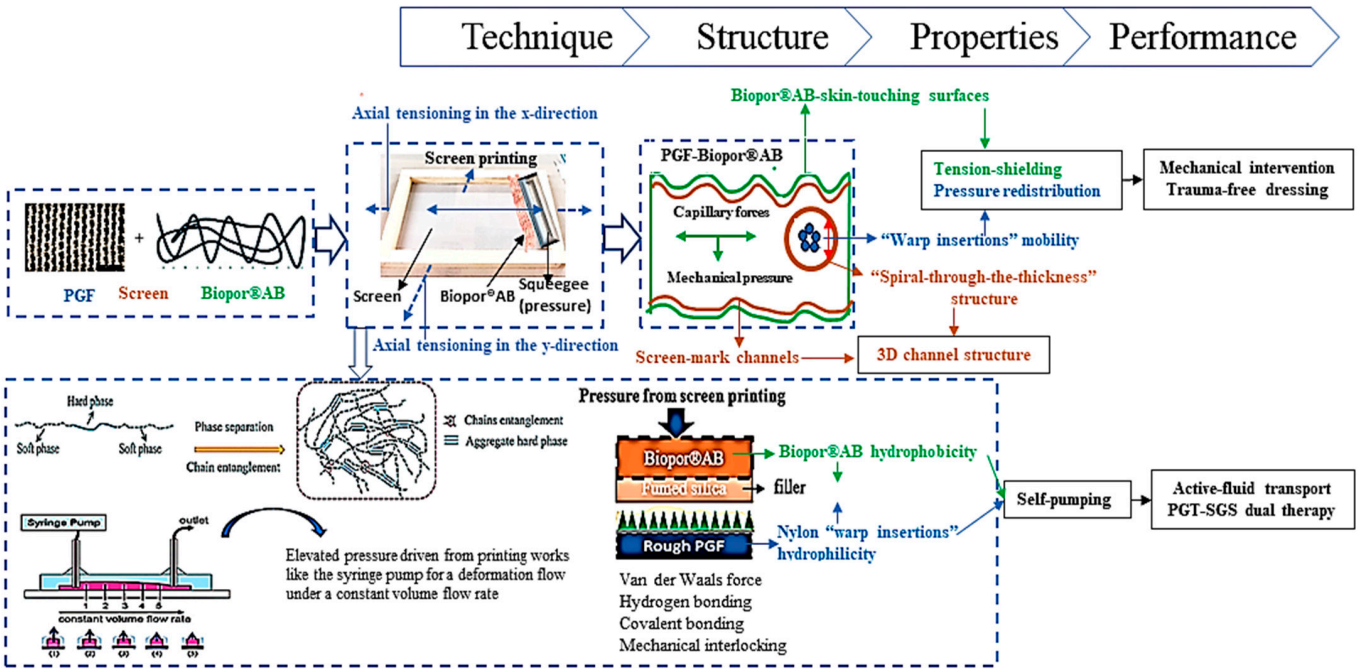

Figure 1. Flowchart for proof-of-concept fabrication of PGF-Biopor®AB composite dressing.

The structure of PGF-Biopor®AB dramatically affects the dual therapy efficacy and hydration performance. The PGT with warp insertion mobility provided compression while the Biopor®AB hydrophobicity performed SGS therapy. This combination achieved efficacy optimization of the therapy. By screen and warp-knit structure applications, we created a 3D channel structure consisting of screen-mark channels and "spiral-through-the-thickness" structures in the same composite. The 3D channel structure and the bubble-connected

microchannels formed the pathways of transport. In this self-pumping dressing, mechanical pressure drives nylon absorptivity as a dynamic enhancer for active-fluid transport. Pore diameter variations in asymmetric surfaces, steps, and spirality allowed the smooth fluid flow to complete the active-fluid vehicles [33–35]. In the self-pumping process for the active-fluid transport, active nylon absorptivity and channels further improve hydration performance with improved water vapor transmission rate (WVTR) and enhanced water uptake capabilities.

2. Materials and Methods

2.1. Materials

PGF is a standard warp-knit fabric with warp insertions—wrapped yarn in nylon 50D/warp insertions in 12SPK filaments with spandex 420D (68% nylon 32% spandex, 210 gm/m^2). PGF (Polliam Trading Corp. Ltd., Hong Kong, China) is a public hospital occupation-use material supplied by the sole supplier. Biopor®AB bought from Dreve Otoplastik GmbH via Widex Hong Kong Hearing & Speech Centre Ltd. Notably, 25 shores Biopor®AB is a medical-grade silicone fulfilling (i) a long history of successful animal and human implantations, (ii) manufactured in pharmaceutically clean conditions, and (iii) a quality-controlled-medical application [36]. Being a developed medical silicone, Biopor®AB guarantees the absence of substances that lead to inflammatory conditions, irritations, allergies, or cell mutation, and the oxygen permeability enables occlusive hydration via dermis contact (without needing direct epidermis contact). For this reason, Biopor®AB can be used in implants, silicone scar sheets, and this PGF-Biopor®AB. The official supplier-provided silicone gel sheeting (Cica-Care®, Smith and Nephew, UK) was used as a control. Screens #1000 (#1000 = 2.54 × 10^4 nm) and #2000 (#2000 = 1.27 × 10^4 nm) in wooden frames of 8″ × 10″ and 14″ × 20″ were used—Tony Screen of Jet T Technology from C1A. G/F, 72 Hoi Yuen Rd, Kowloon, supplied the screens. Aveeno® skin relief moisturizing lotion (Johnson & Johnson Consumer Inc., Skillman, NJ, USA) and filter paper were ordered from Market Place supermarkets. Omnifix® (Paul Hartmann Asia-Pacific Ltd., Hong Kong, China) is a pressure-sensitive adhesive brought from the Prince of Wales Hospital rehab shop.

2.2. Preparation of PGF-Biopor®AB

Hand-screen printing (HSP) was a proof-of-concept fabrication process for the composite dressing. Standard pressure and knife-edged squeegee right-angled positioning were applied to avoid shear-pressure influence on Biopor®AB viscosity. Referencing Gu et al.'s 7% pre-straining data, the warp insertion mobility design was realized at 10% pre-straining [37–39]. The same operator set a contamination-free printing table using paper and plastic sheets lined with water. Standard PGF was 10% biaxial-tension-mounted on a 100% double-taped plastic sheet for screen printing. To achieve the suggested 30-min vulcanization for consistent formality and printability, the same operator adopted an elevated pressure (98 N to 196 N). For best efficacy and patient comfort, a 1–4 mm composite was selected to achieve oxygen-enabled and cell culture performance conditions [34–36]. Samples with a thickness ≤3 mm and sizes 20 cm × 20 cm were prepared. A thin layer set (2, 4, 6, and 8) and a thick layer set (25, 50, 75, and 100) were used in a comparative study. Two screens (#1000 and #2000) were used to evaluate the screen size effect. Printing layers were a key parameter for assessing Biopor®AB deposition. PGF-Biopor®AB samples were labeled as PGF-x-y, where x denoted the number of printing layers, and y denoted the screen#. All as-prepared samples with controls (Cica-care® and PGF) were kept in slit trays under a standard condition at 65 ± 2% relative humidity and 20 ± 2 °C for at least 24 h before measurement and testing [40–43].

2.3. Investigations of Physical and Structural Properties

A Leica digital microscope (M165C with HD290, Leica Mikrosysteme Vertriebs GmbH, Wetzlar, Germany) examined the structural changes. A scanning electron microscope (SEM) Hitachi TM3000 (Angstrom Scientific, Ramsey, NJ, USA) was used to investigate the surface and interfacial morphologies. Pressure measurement was taken with a Microlab© pressure calibrator (Microlab Pico Press®, Microlab Electronica SAS, Padua, Italy). Staining with Dispersol blue (D-2R 3%) or without dye, and with or without pressure, was applied to prepare the samples for observation under the optical microscope (OM). For design verification of self-pumping "warp insertions" mobility and compression therapy, three samples (PGF-2–1000) were pressured between binder clips for 14 mmHg (light, 1 × 25 mm binder clips of 1.15 N) and 21 mmHg (heavy, 2 × 25 mm binder clips of 2.30 N) to simulate the actual pressure of compression. The control set was with no clips (p = 0 mmHg). Contrasting light and heavy compression demonstrated a comparative study.

Pore size by diameter, number of pores, and porosity% were investigated to understand the bubble-connected microchannels. The principles and calibration method for measuring the porosity volume were measured by means of water desorption or mercury intrusion porosimetry. However, both forms of measuring volume for porosity would include PGF open area in the calculations. A larger than bubble-connected microchannel open area would make porosity calculations unreliable. Assuming that pores are uniform and circular, the functional surface apparent porosity, as defined by the International Union of Pure and Applied Chemistry (IUPAC), can be calculated as follows [44]:

$$\text{Functional surface apparent porosity} = (\text{Volume of inner pores})/(\text{Total volume}) \times 100\% = (\text{Pore area})/(\text{Total area}) \times 100\% \quad (1)$$

We determined the water vapor transmission rate (WVTR) for PGF-Biopor®AB (samples), control of PGF (control 1), and Cica-care© (control 2) according to ASTM E96-14 for the water permeability test in cup-method. Each disc-shaped sample of 96 cm^2 was tightly mounted on the top of a cylinder cup containing 46 mL of distilled water. The rough Biopor®AB-skin-touching PGF-Biopor®AB side was placed downwards, facing the water to simulate the vapor transfer from the skin to the environment. Three replicates were performed. Each as-prepared sample was weighed and recorded before and after every 24 h. We calculated water permeability using the water vapor transmission rate (WVTR):

$$\text{WVTR} = \text{change in mass}/(\text{area})(\text{time}), \text{ unit in gm}/\text{m}^2/\text{day} \quad (2)$$

Water uptake was determined by immersing an initial weight (W0) of the dried samples (PGF-Biopor®AB, control of PGF and Cica-care©, Ø = 9.8 cm, 96 cm^2) in distilled water for a different predetermined time (24, 48, 72, 96 h). They were separated from water, wiped dry using a cotton towel, and weighed (Wt). The water uptake wt. (%) for water uptake capability was calculated: Water uptake wt. (%) = (Wt − W0)/W0 × 100.

2.4. Trial Patient Study with ATDDS

An assisted transdermal delivery system (ATDDS) was used for operating self-pumping for PGT-SGS dual therapy and active-fluid transport (Figure 2A). The scarring skin of a burn patient (age 20, 60 Kg, BMI 25, with degree 2 and degree 3 scarring area from the leg) was first applied with a flat layer of 10 mL Aveeno® skin relief moisturizing lotion. The lotion was circularly massaged until it was in full saturation. The massaging pressure was applied from the top without stretching the scarring tissues to avoid the stretching-friction-induced wound. To validate the effectiveness of 10–25 mmHg PGT-SGS therapy, manual elastic bandaging (Figure 2B-1. 1/3, 2B-2. 1/2, 2B-3. 2/3 overlaps) and self-adhesive Omnifix® fixed (Figure 2C) were separately trial assessed before the trial patient study. The Microlab© pressure calibrator was used for pressure evaluation (Figure 2D).

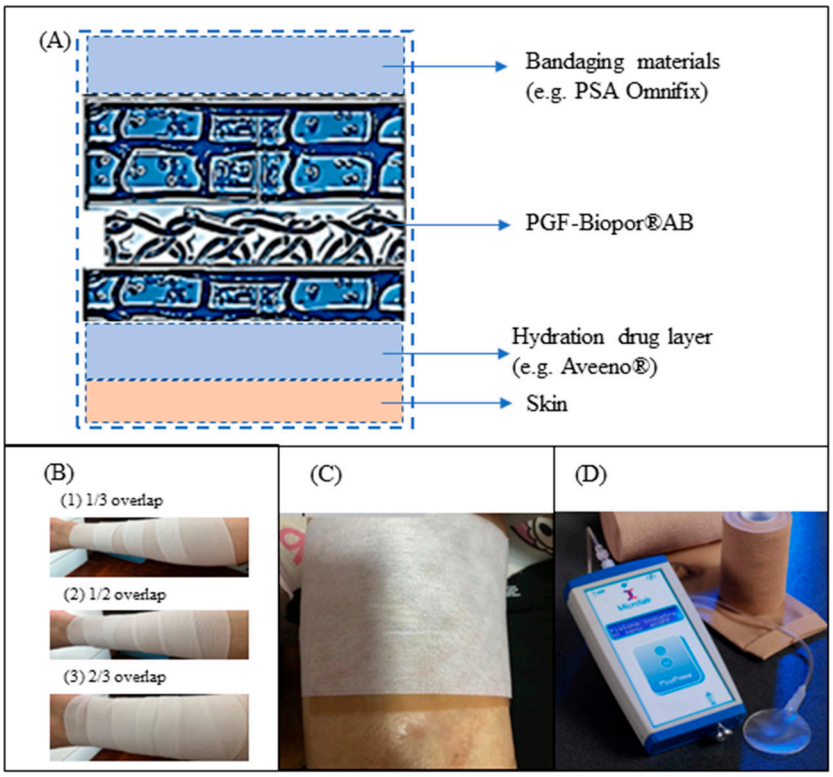

Figure 2. Illustration of ATDDS for PGF-Biopor®AB application (testing pressure levels in 10–25 mmHg): (**A**). ATDDS, (**B**). Different ways of bandaging, (**C**). Omnifix®-fixed, (**D**). The Microlab© pressure calibrator for pressure evaluation.

Vancouver Scar Scale parameters (scar pliability, thickness, irregularity, and color) were adopted for scar performance assessment. Zones 1 and 2 were large-area degree-2 and degree-3 scarring sites selected from the leg. Both samples and control were taken on adjacent scarring skins for easy comparison. In the empirical trial patient study, PGF-Biopor®AB was applied (PGF-50-1000 for Zone 1 and PGF-6-1000 for Zone 2) on the scarring tissue before 20 mmHg bandaging at 1/2 overlap for daily treatment of 4–8 h. After every predetermined time (7, 14, 21, and 28 days), samples with control (no treatment) in ATDDS were iPhone photo-imaged to assess the scar-healing efficacy. The same ATDDS concept was also applied in the WVTR simulation test. A flat layer of 5 g of Aveeno® skin relief moisturizing lotion was first spread between PGF-Biopor®AB and a filter paper before Omnifix® adhered to PGF-Biopor®AB. The rough filter paper side was placed downwards, facing the water to simulate the vapor transfer from the skin to the environment.

3. Results and Discussion

3.1. Dressing Structure

3.1.1. Warp Insertion Mobility

A warp insertion mobility design aims for mechanical pressure-driven self-pumping for PGT. Different mechanical pressures can activate different unidirectional warp insertion movements. Light/heavy stress and no stress (for control) developed different compressive resistances to drive different warp insertion mobilities for various internal structural-dimensional changes in the through-the-thickness plane. The cross-sectional OM images of a PGF-2-1000 sample were used (Figure 3) to show the different structural changes with different levels of pressure to verify the "warp insertions" mobility design. A0, X0, Y0, A1, X1, Y1, A2, X2, and Y2 denoted the relative movements of the warp insertions.

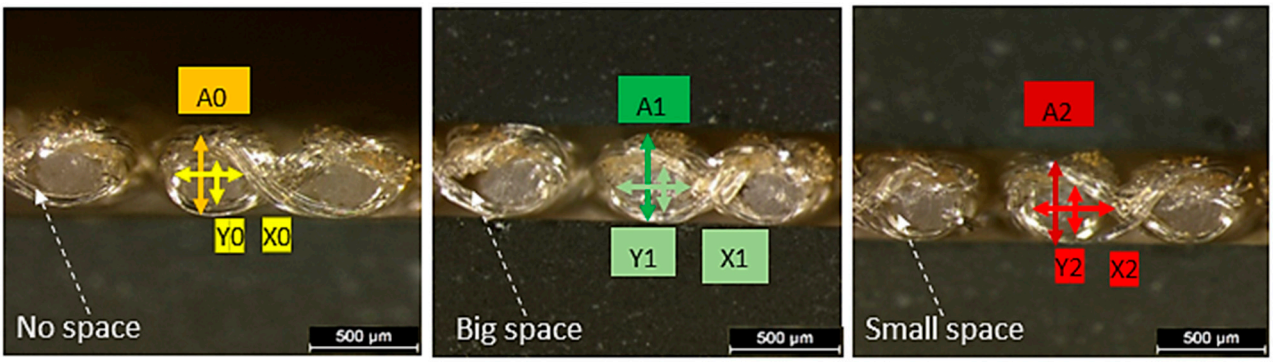

No compression:	Light compression:	Heavy compression:
(P=0 mmHg)	(P=14 mmHg)	(P=21 mmHg)
A0=381 µm	A0=374 µm (−1.8%)	A0=382 µm (+0.3%)
X0=212 µm	X0=225 µm (+6.3%)	X0=205 µm (−3.3%)
Y0=286 µm	Y0=283 µm (−10.5%)	Y0=305 µm (+7.7%)

Figure 3. Illustration of mechanical pressure-driven "warp insertions" mobility for self-pumping: the cross-sectional OM images (PGF-2-1000) illustrated the structural changes under different mechanical pressures (pressure measurement using Microlab© pressure calibrator).

For PGT, pressure garments were made smaller than the actual body garment circumference by circular stretching on the PGF-tension-sharing loops to provide compression [45]. In PGF-Biopor®AB architecture, the biaxial (warp-wise and weft-wise) tensioning conditioned with no fiber orientation in the tension-sharing loops. In a normal condition before pre-straining, the yarn extension straightened the warp insertions with a low yarn tension on the loops, constituting a "helical shape" [46,47]. Increasing the pre-straining would cause a higher density packing of loops until maturation [37–39,46,47]. At maturated biaxial tensioning, the biaxial tensioning exerted uniform pressure to reallocate yarn spaces for a "parallel-pile-up" loop state. The "parallel-pile-up" tightly packed loops functioned as closed doors to allow no Biopor®AB impregnation and retain structural warp insertion mobility [46–48].

The "warp insertions" are free to move under pressure when the mobility design causes force transmission from the wrapped yarn (the loops) to the nylon core yarn ("warp insertions") to be negligible. Upon application of different mechanical pressures, different structural changes results, e.g., a larger space was observed under light pressure (p = 14 mmHg, a 6.3% extension in the X-direction and a 10.5% contraction in the Y-direction). A smaller space was observed under heavy pressure (p = 21 mmHg, a 3.3% contraction in the X-direction, and a 7.7% extension in the Y-direction). Under biaxial tensioning with no Biopor®AB impregnation, the bundles of warp insertions were enclosed inside Biopor®AB-wrapped loops of "spiral-through-the-thickness" structure such that "warp insertions" were free to move under mechanical pressure. This pre-strained biaxial tensioning enables a tailorable self-pumping configuration. The pressure-driven warp insertion mobility served as the engine for PGT, and active nylon absorbency dynamically enhanced active-fluid transport [48–51].

To further assess the range of compression therapy, two samples (PGF-6-1000 and PGF-50-1000) were ATDDS burn-patient-applied using two different methods (PSA Omnifix® and elastic bandage methods). In this study, both approaches confirmed compression therapy offering two different pressure ranges for selection: (i) PSA Omnifix® achieved 10–15 mmHg and (ii) elastic bandaging with tension and overlapping achieved 10–25 mmHg. The created Biopor®AB-skin-touching surfaces demonstrated SGS and a below 25 mmHg PGT is verified; the PGT-SGS dual therapy realized simultaneous application in the same composite. The ATDDS PGF-Biopor®AB application at 10–25 mmHg demonstrates an innovative and user-friendly way of treatment, simultaneously saving the need for a secondary dressing

and solving the problem of patient discomfort at above 25 mmHg and the issues for patient compliance [30,52].

3.1.2. Structure of Biopor®AB-Touching-Skin Surfaces

Planar-screen-print pressure had PGF embedded into Biopor®AB layers, offering PGF-Biopor®AB silicone-skin-touching surfaces. The coating of microscale nylon mesh provides potential deposition sites for cell lysis and temporary coverings for scar sites [53]. Biopor®AB hydrophobicity at outer surfaces temporarily provides bacterial exclusion and moisture loss control [53]. The lower applied pressure (10–25 mmHg) PGT with silicone skin-touching surfaces eliminated the PGT drawbacks of friction-induced wounds and discomfort experienced at pressures above 25 mmHg. Upon PGF stretching (Figure 4A–C), tensioning loops created thin, sharp edges that caused friction-induced wounds in the scarring tissue. At a pre-strained conditioned "parallel-pile-up" loops (Figure 4D–F), Biopor®AB-wrapping offered Biopor®AB-skin-touching surfaces with blunted and smooth edges. The PGF embedding as reinforcement could provide external mechanical support to facilitate tensile shielding.

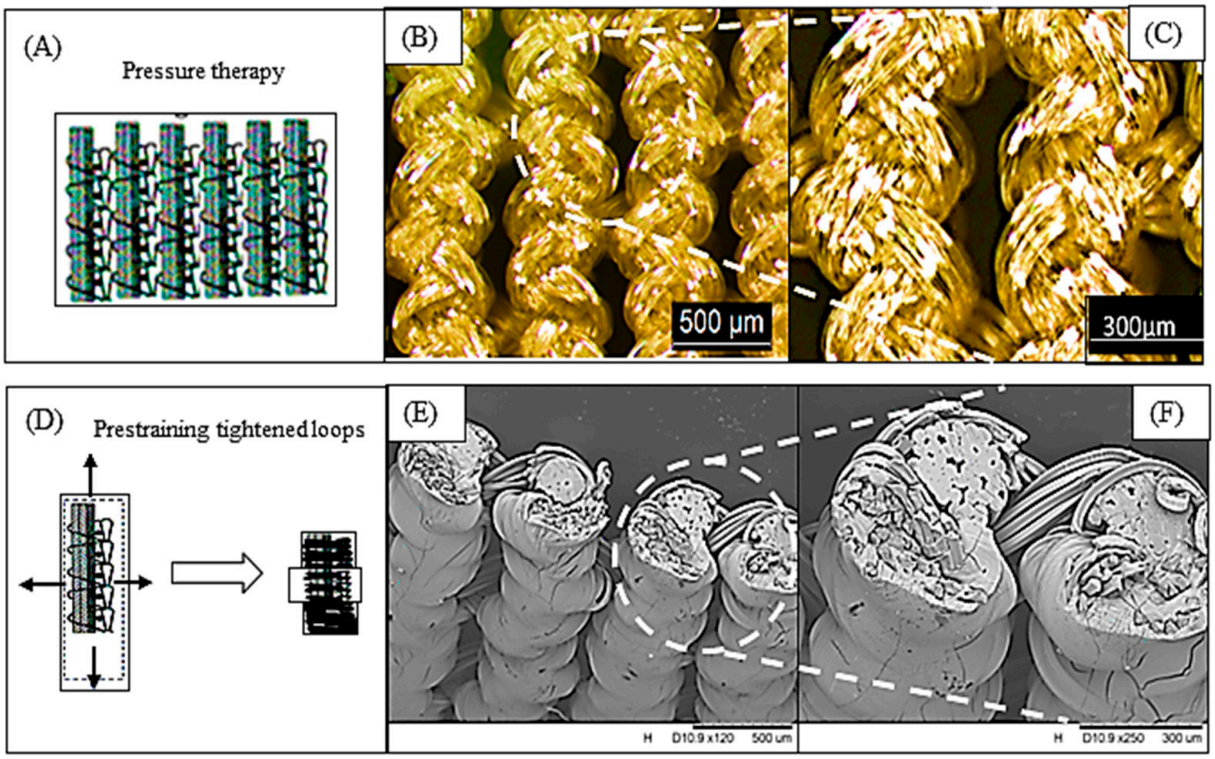

Figure 4. Contrasting of a PGF at compression therapy and PGF-Biopor®AB structure: (**A**). Sketch of PGF, (**B**). PGF (OM 120×), (**C**). PGF (OM, 240×), (**D**). Illustration of pre-strained tightened loops to "parallel-pile-up" loops, (E). PGF-Biopor®AB (PGF-2-1000, SEM in 120×), and (**F**). PGF-Biopor®AB (PGF-2-1000, SEM in 240×).

Similar to other silicone membranes and tension-shielding elastomeric biomaterials, the tension relaxation properties of Biopor®AB silicone skin-touching surfaces provide pressure-relieving surfaces for tension shielding—both functions for scar reduction [54]. Shear and friction forces cause friction-induced wounds. Replacing Biopor®AB-skin-touching surfaces and structure with "warp insertions" mobility enables pressure redistribution, the least tissue pressure/force achieved cell-contact pressure-releasing effect. The pressure-driven warp insertion mobility for self-pumping allows alternating pressure shifts; the Biopor®AB 3D isotropic properties enabled pressure redistribution for stress-strain reduction and shear-releasing [25,54]. Thus, upon self-pumping, the enlarged contact areas

eliminate high-pressure points and allowed dynamic pressure redistribution for shear-friction reduction. The pre-strained Biopor®AB-coating, therefore, modified the interfaces' composition, structured for pressure redistribution and mechanical stress control, achieving scar therapeutics efficacy [29,30,37,38,44–46,55–57]. The uniformly adhering structure also helps to avoid fluid-filled pockets where bacteria would otherwise proliferate [16]. Pain-free dressing removal helps protect against damage to the regenerating epidermis or granulation tissue [16].

3.1.3. 3D Channel Structure

Silicone impermeability can cause skin irritation and inflammation, and plastic surgeons do not recommend Cica-care© for non-healed scarring wounds. The 3D channel structure, microscale channel pathways were intentionally built for diffusion routes to increase permeability and anchoring sites for cellular scar healing. The OM longitudinal images in Figure 5A revealed a breakdown of the 3-D channel structure: (i) distorted Biopor®AB-printed screen-mark channels in the x-y plane and (ii) stair-steps and spirality in a "spiral-through-the-thickness" structure with bubble-connected microchannels located in the y-z plane. The OM cross-sectional image in Figure 5A revealed that PGF-Biopor®AB had Biopor®AB-coated asymmetric Biopor®AB-skin-touching surfaces and a "spiral-through-the-thickness" structure linking from a smooth technical face (TF) to a rougher technical back (TB). SEM images in Figure 5B displayed the inside of this "spiral-through-the-thickness" structure. Each stair step measured approximately 100–300 µm with spirality formed from the "parallel-pile-up" loops. The microscale Biopor®AB-coated 3D channel structure was obtained from the screen gauge and Biopor®AB-wrapping on warp-knit stitching loops. The microscale channels and "spiral-through-the-thickness" structure offered diffusional transport routes that increased water vapor permeability; the microscale roughness of the 3D channel structure provided anchoring sites for bioactivity to improve cell adhesion, cell infiltration, and attachment [53].

In engineering PGF-Biopor®AB for breathability and comfort, the PGF textile structure was applied to moisture permeability, water storage, and moisture transfer capability [55–57]. The textile structural design typically has large specific areas of 10^2–10^3 m^2/kg, various porosity levels, and structurally defined fiber volume fractions for permeability and comfort [55–57]. By warp-knit structure application, biaxial tensioning conditioned "parallel-pile-up" loops to print a "spiral-through-the-thickness" structure [35–39,45,46]. Each loop formed a stair step, and the connection of parallel-tightly packed loops yielded spirality. The yarn loop size decides the height of the stair step, and the level of pre-straining determines the structure's spirality. The screen-mark channels were created by screen application. Biopor®AB is a two-part room temperature vulcanization (RTV2) formulation. The immediate curing function of the condensation reaction allowed the Biopor®AB to be quickly set in the screen-mark channels.

Additionally, air bubbles formed in Biopor®AB under the pressure of the squeegee. Under planar pressure compressing, bubbles were centre-crushed and pressure-pushed into the "spiral-through-the-thickness" structure in the planar pressure direction. Under close connectivity, Biopor®AB pressure-connected the centre-crushed bubbles into random lengths of microchannels. Screen-mark channels, the "spiral-through-the-thickness" structure, and bubble-connected microchannels formed the diffusional pathways of the active-fluid transport. The 3D channel structure provided routes for diffusional fluid flow, breathability, and anchoring sites for bioactivity.

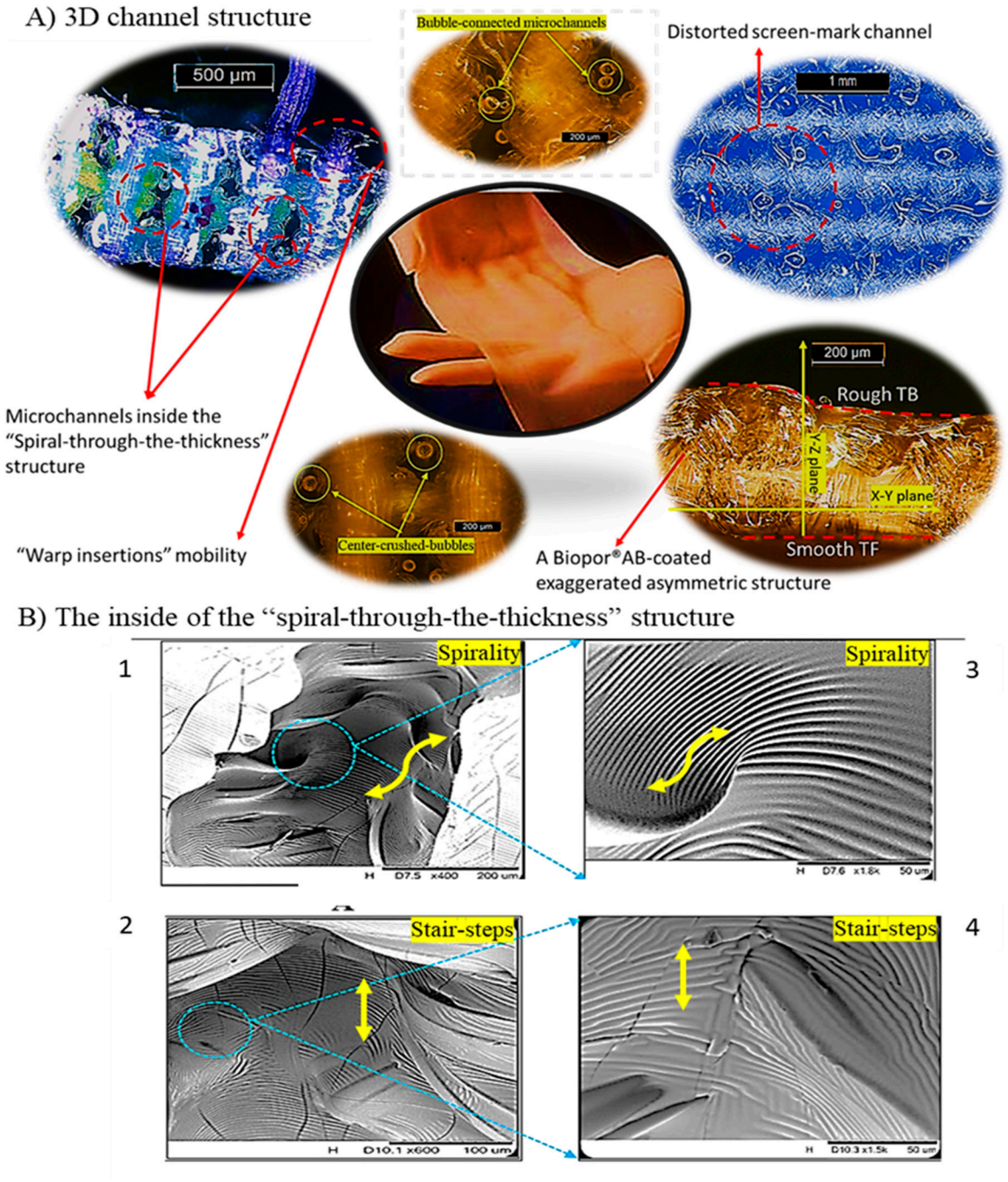

Figure 5. OM and SEM images of PGF-Biopor®AB (PGF-50-2000 sample) displayed (**A**) The 3D channel structure and (**B**) The inside of the "spiral-through-the-thickness" structure: (**B1**). SEM technical face view (400×), (**B2**). SEM technical back view (600×), (**B3**). SEM technical face in high resolution (1800×), and (**B4**). SEM technical back in high resolution (1500×).

3.1.4. Active-Fluid Transport

Self-pumping is realized by combining the Biopor®AB hydrophobicity with the nylon warp insertion hydrophilic characteristics. The warp insertion mobility functioned as the engine of self-pumping, with the 3D channel structure provided the transport pathways, asymmetric gradient surface roughness structured a directional water transfer to complete active-fluid transport. The process of self-pumping demonstrated continuous hydration by active-fluid transport that prevented reverse osmosis from the scarring site [27–29] (Figure 6A). Wang et al. first reported the directional water transfer through fabric-induced

asymmetric wettability [58,59]. Integrating a woven-knitted bifacial structure created an asymmetric fabric structure for asymmetric wettability [60]. Similar to the bifacial fabric design, the inherent warp-knit-asymmetric PGF structure provided a platform for asymmetry in Biopor®AB-coatings. Pressure-induced chemical interactions via the carbonyl and hydroxyl groups of Biopor®AB increased interfacial bond strength on the fibre surfaces for strong fibre-matrix adhesion (Figure 6: B1. Van der Waals force, B2. Hydrogen bonding, B3. Covalent bonding, B4. Mechanical interlocking). The RTV2 formulation of Biopor®AB comprises addition and condensation reactions (Figure 6C). The platinum crosslinking catalyst (Pt) and water from the air (H_2O) produced siloxane bond rearrangement. The RTV2 formulation, filler and planar-pressure-induced mechanical interlocking exerted gradient interfacial adhesions, forming a heterogeneous asymmetric structure on TF and TB. The material of weak interfacial adhesion at TF yields low surface roughness for a smooth technical surface [61]. In contrast, a robust interfacial adhesion produces a high surface roughness for a rougher TB. The gradient surface roughness of different surface areas resulted in the observed heterogeneous asymmetric structure [56,57,62–65]. This asymmetric gradient surface roughness at TF and TB provided the gradient wettability for a directional water transfer [65].

Self-pumping warp insertions use mechanical pressure and capillary forces to physically enhance the fluid directional flow. Figure 6(D1) illustrated that the screen-mark channels and the "spiral-through-the-thickness" structure with steps and spirality provide a diffusional pathway for directional water transfer. The self-pumping process allowed active-fluid transport, and the fluid could be transferred from the screen-mark channels to the rougher TB. We can use the water flow mechanism of a waterfall fountain (Figure 6(D2)) to explain the unidirectional fluid flow in the steps and spirality of the "spiral-through-the-thickness" structure. A PGF-50-1000 sample is pressure-dyed between clips and pathways of screen-mark channels, and the "spiral-through-the-thickness" structure can be blue-dyed in Figure 6(D3). These blue-dyed pathways verified the active-fluid flow mechanism and provided evidence for directional fluid flow in the 3D channel structure.

Benchmarking the studies by O'Connor, Comanns, and McNeely, different fluid flow restrictions could be made by variations in the diameters of channels and microchannels [41,66,67]. The diameter variations in the screen-mark channel and the steps and spirality in a "spiral-through-the-thickness" structure facilitated even flow in the 3D channel structure. Referencing McNeely's hierarchical channel structure, the variations in the diameters can facilitate greater transport distance, constituting a longer duration of fluid travel [41]. The self-pumping by pressure-driven "warp insertions" mobility helped to smoothen the fluid flow without any resistance and blockage within the 3D channel structure [68]. The path's topologic diameter variation primarily smoothed diffusional flow and retained water [41]. Thus, we believe an active directional transfer fulfils hydration with water retention for an ideal burn dressing and scar therapeutic that also provides a proper fluid balance that helps to avoid an increase in metabolic rate and a fall in temperature [16].

3.2. Physical Properties

3.2.1. Water Uptake Capability

In assessing the water transport properties of textiles, the water uptake wt. % indicated transport rates and surface wetting time for the ability of water transfer illustrates the 3-day water uptake wt. % curves of PGF-Biopor®AB with control of Cica-care© [65] Figure 7. Compared to the Cica-care© (1.18%), the as-prepared samples (1.59–13.09%) showed a significant improvement in water uptake capability over 3-days. The initial rate of water absorption was linear for all as-prepared composites. After extending the immersion time, the % of water absorption slowed and approached a saturation stage. Therefore, all water absorption behavior follows a Fickian diffusion process [69]. Comparing the thin layer set (8.85–13.09%) to the thick layer set (3.23–6.57%), the thin layer set (#1000 and #2000) demonstrated a two-fold improvement in water uptake capability. This significant

improvement in water uptake may be due to the active nylon warp insertion absorbency and spaces for warp insertion mobility under pressure.

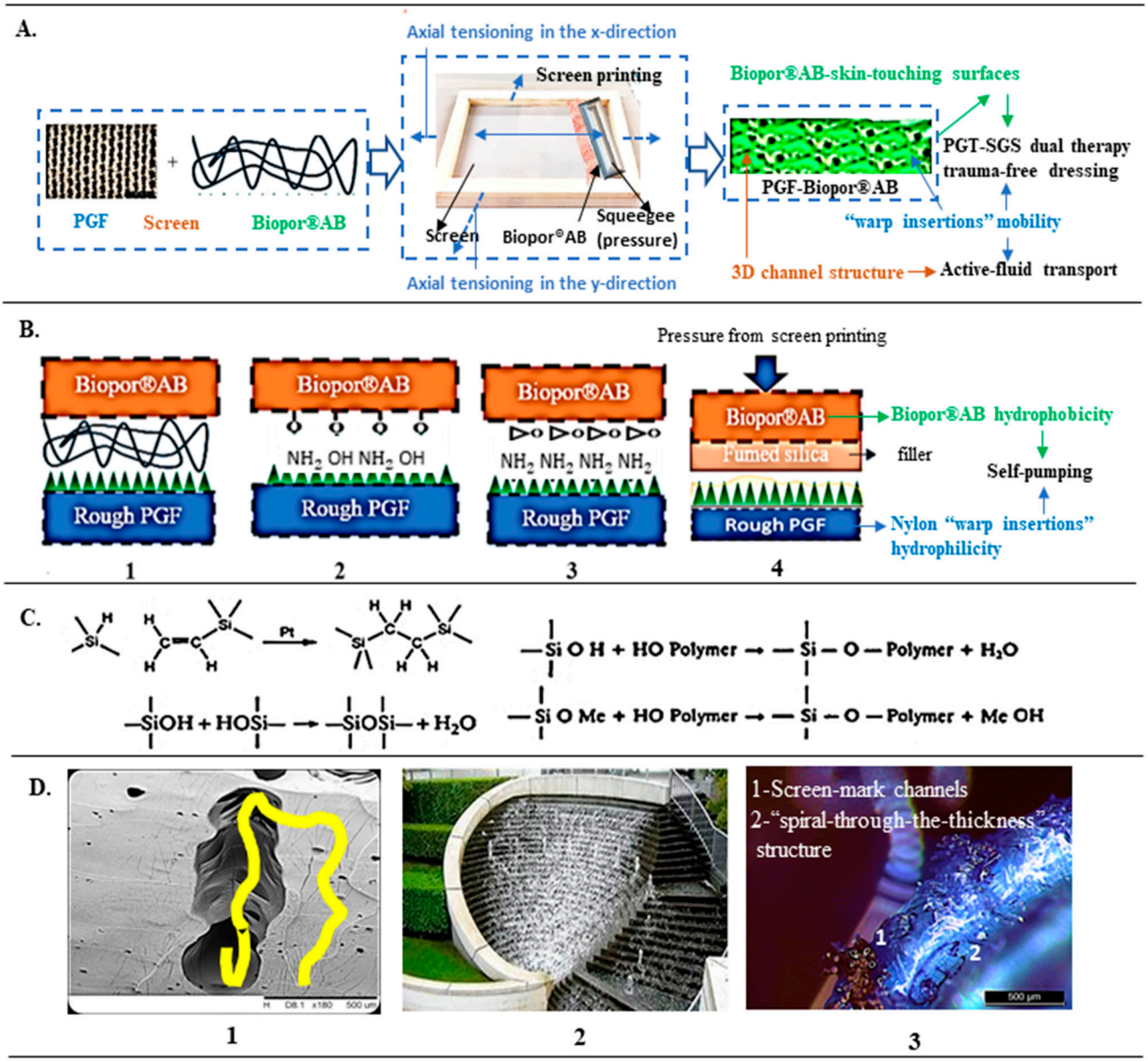

Figure 6. Structure design and properties of self-pumping dressing: (**A**). Fabrication, (**B1**). Van der Waals force, (**B2**). Hydrogen bonding, (**B3**). Covalent bonding, (**B4**). Mechanical interlocking, (**C**). Chemical reactions of addition and condensation, (**D1**). A diffusional pathway (SEM image), (**D2**). A water-fountain mechanism for diffusional transport, and (**D3**). Evidence (OM image of a pressure-dyed PGF-50-1000).

Principally, water travels by capillary action [70]. Large capillaries, in general, produced higher wicking rates. Here, the self-pumping pressure affects the nylon absorbency and the microscale details of the diffusional pathways, which affect the water transport rate. The printing layers affect the composite thickness. Figure 8 illustrated a linear correlation between composite thickness^2 (T^2) and the number of printing layers. For warp insertion mobility reduction with increasing thickness, both the liquid sorption within fibers and swelling of fibers caused a reduction in space for capillary penetration [71]. The decreased mobility further declines the volume of liquid flowing in the areas. Nylon fibers also inhibit

fluid movement, which causes a blockage of inter-fiber capillary action for a lower dressing water absorptive capability [71].

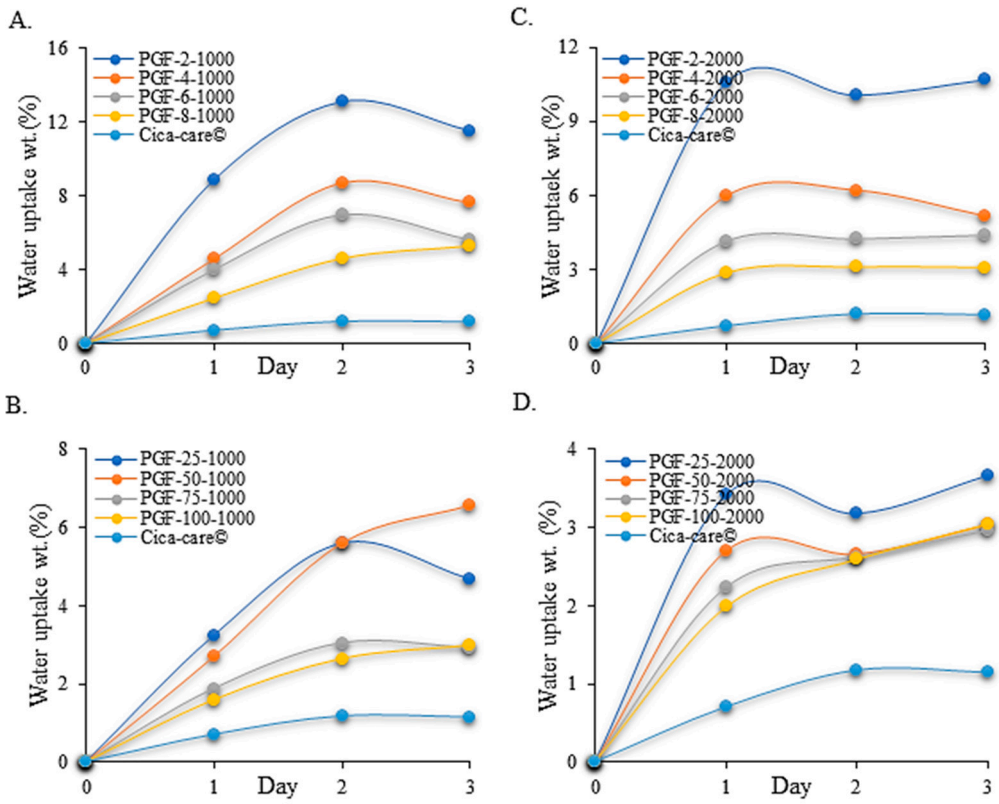

Figure 7. Notably, 3-day water uptake capability curves for different as-prepared samples in #1000 and #2000 (**A**,**C**). Thin layers 2–8, (**B**,**D**). Thick layers 25–100 [PGF-x-y, x denotes the number of layers of Biopor®AB printed on a single layer of PGF, y represents the # of screen sizes].

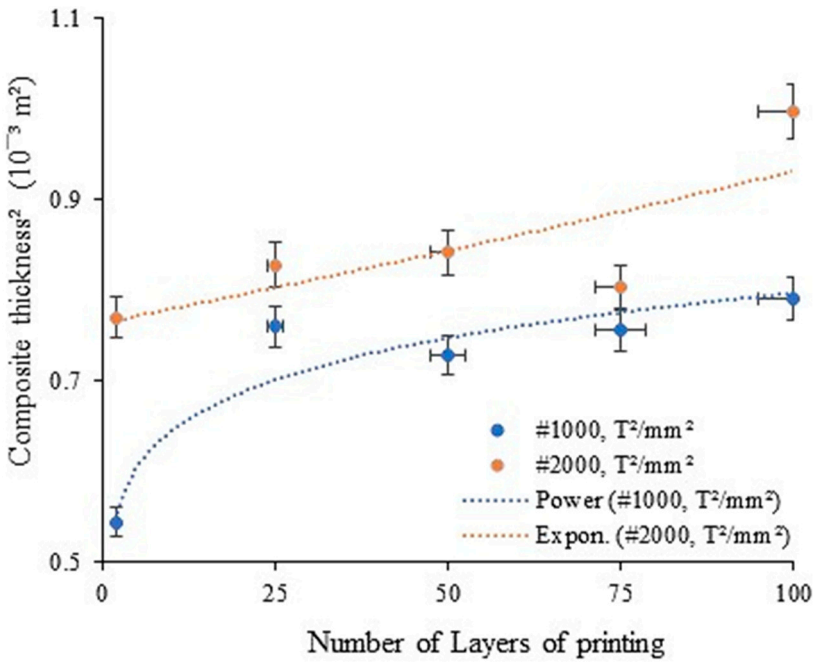

Figure 8. Correlation of composite thickness^2 (T^2) and the number of layers (selective samples in #1000, y = 0.52 × $^{0.092}$, R^2 = 0.91 and #2000, y = 0.76e$^{0.002x,}$ R^2 = 0.61 in moderate to strong correlation).

Nylon is semicrystalline and the most hydrophilic synthetic fiber. The amide groups in nylon can form hydrogen bonds with water for the sites of water sorption [72]. The additional printing layers provided extra layers of Biopor®AB-wrapping for thickness resulted in decreased spaces for warp insertion accommodation and caused a reduction in mobility. Therefore, a thinner coating thickness allows more spaces for warp insertion mobility, nylon absorbency, and higher absorptive capability. Similar to the absorption concept in PLA-coated sisal fiber-reinforced polyester composite, the thickness increase with printing layers should keep nylon fibers in warp insertions isolated from water absorption [69]. The Biopor®AB-coating thickness directly impacts the absorption effect; the two-fold water uptake capability for the thin layer set over the thick layer set explains the influence of Biopor®AB-coating on the absorption effect. Increasing Biopor®AB-wrapping made them more hydrophobic and reduced nylon warp insertion mobility—both decreased water absorption [68]. The hydrophobic–hydrophilic gradient structure increased hydrophobicity and reduced warp insertion mobility with growing layers, which explains the reduction in water uptake capability.

Apparent porosity (%) and pore size by diameter with uniformity and distribution were used for microchannel size investigation. As Table 1 illustrates, a microscale range by size for microchannels was obtained. The spectra by microscale indicated the random-size inherence from air bubbles. Comparing the screen-mark channels and open spaces of the "spiral-through-the-thickness" structure, microchannel size influence on the rate of water transport can be negligible. The reduction in warp insertion mobility and the absorptivity of nylon fibers can explain the lower water uptake wt. % in the thick layer set [73].

Table 1. Bubble-connected microchannels in apparent porosity (%), pore size by diameter, uniformity, and distribution for microchannel details.

Sampling Groups	Apparent Porosity/%	Diameter of Average Pore Size/μm	S.D. for Pore Size Uniformity	# of Pores for Pore Distribution
HSP–2–1000	0.35	47	0.019	83
HSP–4–1000	0.085	31	0.011	48
HSP–6–1000	5.44	41	0.013	130
HSP–8–1000	0.47	47	0.017	115
HSP–25–1000	0.22	41	0.015	73
HSP–50–1000	0.33	35	0.010	156
HSP–75–1000	0.52	67	0.020	66
HSP–100–1000	0.14	43	0.013	44
HSP–2–2000	0.35	47	0.019	86
HSP–4–2000	0.45	55	0.026	74
HSP–6–2000	0.37	51	0.017	78
HSP–8–2000	0.20	40	0.011	70
HSP–25–2000	1.03	58	0.019	170
HSP–50–2000	0.64	56	0.028	101
HSP–75–2000	1.63	59	0.021	260
HSP–100–2000	1.19	67	0.029	139
Range analysis	0.085–5.44	31–67	0.010–0.029	44–260

We conclude that water uptake capability originated from the nylon warp insertion absorbency and is mobility dependent (or coating thickness^2 dependent). The orderly distribution of the "spiral-through-the-thickness" structure determined the extent and regularity of surface roughness. The steps and spirality supported the capillary continuity for results of water uptake capability improvement [72]. Such steps and spirality, channels and microchannels lengthened travel pathways, and active nylon absorbency from self-pumping functioned like movable "containers" that further improved moisture transfer capability and water storage. In fulfilling an ideal burn dressing, active nylon absorbency with channels and microchannels improved water permeability and uptake capability, providing a humid scarring site that encouraged granulation and assisted epithelization [16].

PGF-Biopor®AB, therefore, not only realizes PGT-SGS dual therapy but also establishes a new concept of active-fluid transport for scar therapeutics.

Comparing the literature data of GT-DA and GT fibrous hydrogel (20%), and absorbent binder and absorbent dressing (around 15–20%), the close to the absorbent binder and absorbent dressing water uptake range demonstrated a high potential of water uptake capability [69]. Compared to Cica-care© (1.18%) and the literature data of commercial Mepiform® silicone dressing (5%), respectively, this favorable water uptake 8.85–13% in thin layer set shows 750–1100% and 177–260% water uptake improvements [69]. Hence, this fair and sustainable water uptake wt. % improvement should be in favor of moisture management for scar therapeutics.

3.2.2. Water Vapor Permeability

Active hydration with water retention is believed to create a moist microenvironment to accelerate scar healing with enhanced cell migration. Active nylon absorbency is achieved via pressure-driven warp insertion mobility, and active hydration with water retention assists in the proper control of evaporative water loss from the scarring site [74]. In the water permeability test of PGF-Biopor®AB with Omnifix© only, a WVTR improvement for #1000 (37.50 to 223.33 g/m^2 per day) and a reduced WVTR for #2000 (34.09 to 107.39 g/m^2 per day) were recorded (Figure 9A,B). In the range of 34.09 to 223.33 g/m^2, 2 samples (PGF-2-1000 and PGF-4-1000) achieved an up-to-normal skin WVTR rate (204 $\pm$ 12 g/m^2 per day) and were almost the same as an ideal wound dressing SRM-B (229.10 g/m^2 per day) [54,73]. Further, both the WVTR requirements of bandaging dressing (200–250 g/m^2 per day) and occlusive dressing (<840 g/m^2 per day) were met. Compared to Cica-Care© (12.75 g/m^2 per day), it was 267% to 1752% higher in WVTR. This result of increasing WVTR from #1000 and reducing WVTR from #2000 with Omnifix© should alert us to the careful choice of bandaging material in ATDDS for the PGF-Biopor®AB application.

An ideal wound dressing SRM-B can help prevent excessive dehydration and exudate build-up without risking dehydration [53]. The up-to-normal skin WVTR could supply a moist microenvironment for scar healing without exudate accumulation [53,75]. PGF-Biopor®AB can carry the same function as SGS to enable a decrease in skin trans-epidermal water loss (TEWL) over time for scar therapeutics [76]. In addition to nylon absorbency for water uptake capability, the increased hydrodynamics of capillary flow by the neighborhood of the microchannels should assist adjacent fluid pathway connections that further enhance WVTR. Increasing printing layers increased both the mass of Biopor®AB and caused an increase in coating thickness, structurally affecting warp insertion mobility. Therefore, PGF- and Biopor®AB-related structural parameters in Biopor®AB mass gain and PGF fiber volume fraction change should help identify the structural influence factors of WVTR. From a further investigation on Biopor®AB mass gain and PGF fiber volume fraction change with WVTR, linear correlations were found for #1000 and #2000 (Figure 9C–F). We can conclude that Biopor®AB mass gain and PGF fiber volume fraction are the critical structural influence factors for the WVTR.

As Figure 10 illustrates, all the 4-day WVTR profile curves demonstrated similar trends to that of the Cica-care© control material. The problem of reducing WVTR over time for PGF (control) was not observed. Similar to the water absorption curves, the initial rate of WVTR was linear for all composites. After extending the immersion time, the rate of WVTR slowed down and approached the saturation stage. With trends of all curves similar to the Cica-care© WVTR profile curves with 4-day WVTR sustainability, the results reflect a dominance of silicone characteristics in PGF-Biopor®AB. The active nylon absorbency contributed to WVTR sustainability; the active nylon absorbency supports a continuous 4-day ATDDS for the PGF-Biopor®AB application.

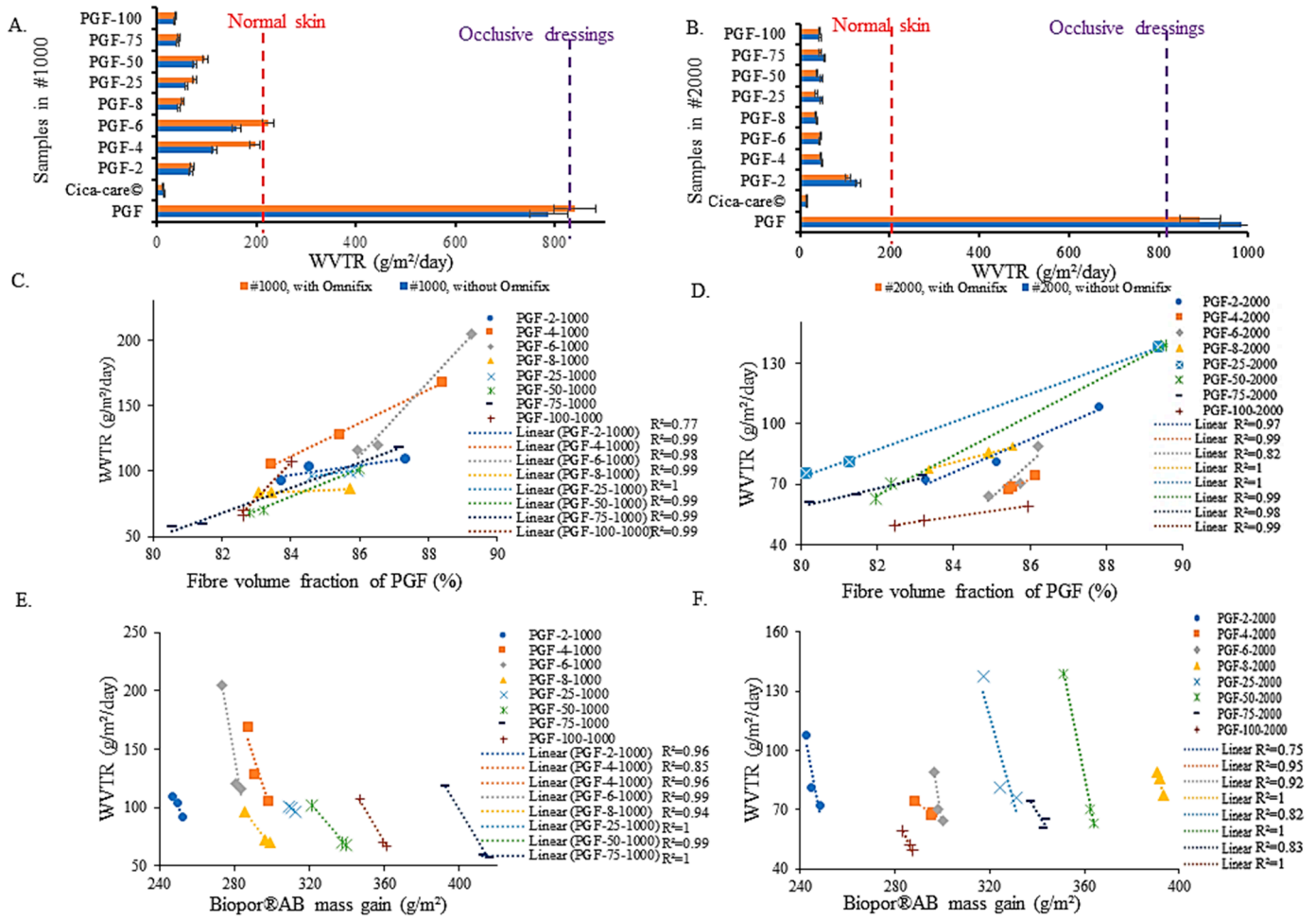

Figure 9. Water vapor transmission rate (WVTR) for different as-prepared samples: (**A**,**C**,**E**). #1000; (**B**,**D**,**F**) #2000; A/B. With and without Omnifix©; (**C**,**D**). Fiber volume fraction of PGF (%) (**E**,**F**). Biopor®AB mass gain (g/m^2) [PGF-x-y, x denotes the number of layers of Biopor®AB printed on a single layer of PGF, and y denotes the # of screen sizes].

Self-pumping dressings establish a new concept of active hydration and active-fluid transport for dynamic silicone occlusive healing theory. Referencing occlusive dressing and silicone clinical efficacy, PGF-SGS dual therapy and active-fluid transport improved hydration performance across WVTR and water uptake capabilities, sustainably offering PGF-Biopor®AB the ability of dynamic hydration with water retention for scar therapeutics. Biopor®AB-enabled oxygen permeability stimulated higher oxygen tension for hydration, increasing the angiogenesis rate and tissue growth [77]. PGT-SGS dual therapy further increased hydration for flattening and lightening the hypertrophic scar by increased capillary activity and localized collagen deposition [77]. Active nylon absorbency performed dynamic water absorption with water retention, which should assist in the differentiation of keratinocytes, the release of cytokines, and the growth factors within the ECM for improved scar healing. Similar to the function of occlusive hydration, active hydration should result in a decreased activation of keratinocytes for reduced production of macrophage cells (IL-1ß and other cytokines) and increased production of antifibrotic tumor necrosis factor (TNF-δ) for an increase in transforming growth factor (TGF-ß3) [40,42]. The combined effect of occlusion and hydration achieved PGT-SGS efficacy optimization, while active-fluid transport should facilitate fibroblast proliferation and collagen inhibition for scar treatment [77].

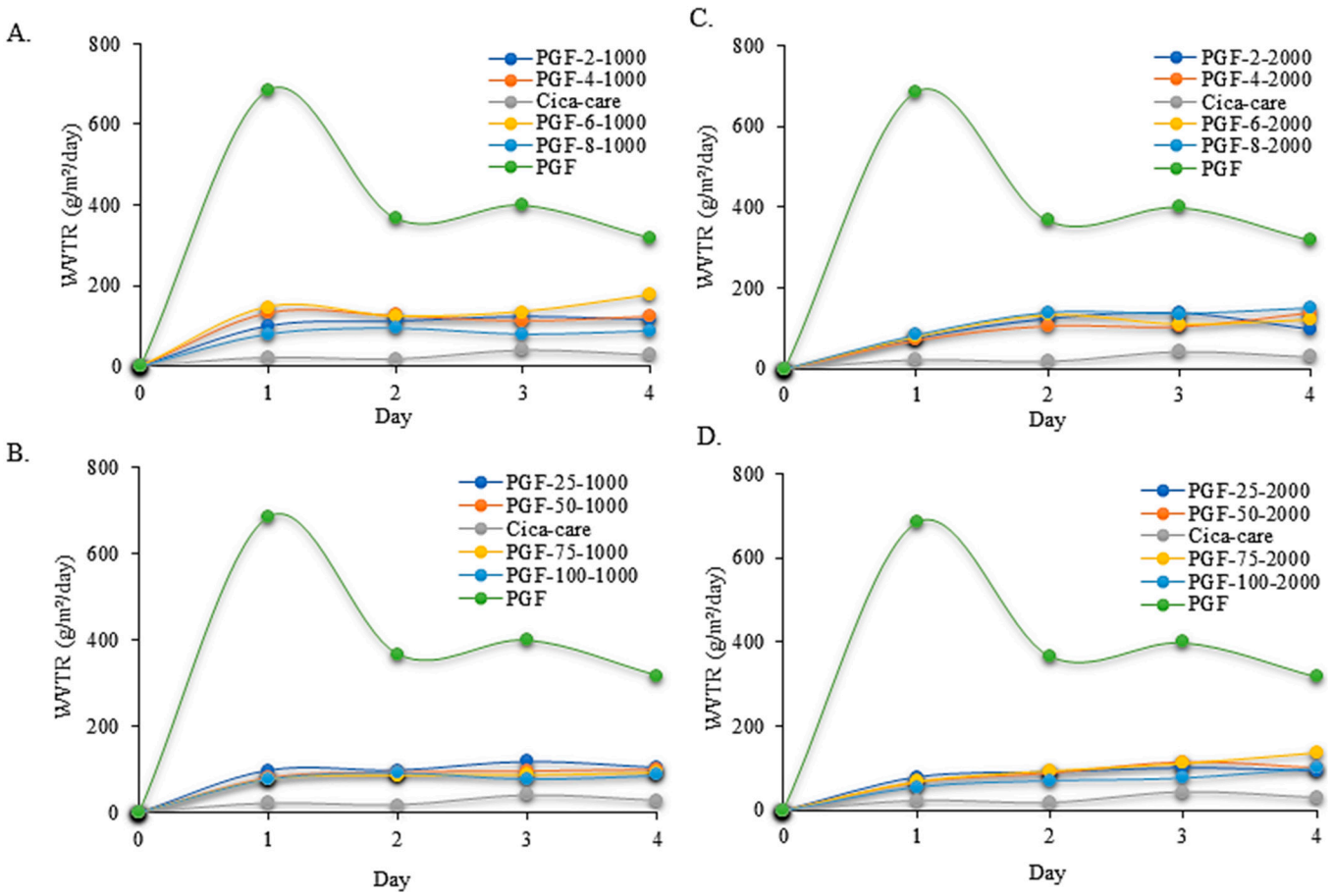

Figure 10. Notably, 4-day WVTR curves for samples with Omnifix© and Aveeno®: (**A**,**B**). #1000; (**C**,**D**). #2000; (**A**,**C**). Thin layers 2–8; (**B**,**D**). Thick layers 25–100 [PGF-x-y, x denotes the number of layers of Biopor®AB printed on a single layer of PGF, y denotes the # of screen sizes].

Applying the data of occlusive dressings, moisture-retention can be expected to heal wounds an average of 3–4 days faster [78]. Referencing occlusive dressing studies with the infection rate of non-occlusive dressing (7.1%), PGF-Biopor®AB, as an occlusive dressing, should record a lower overall infection rate (2.6%) [78]. Using occlusive and non-occlusive dressing data, the falling in an occlusive dressing range should offer a re-epithelialization rate increase of 30–50% and a collagen synthesis increase of 20–60% [78]. With silicone occlusion and hydration, PGF-Biopor®AB should not increase the incidence of clinical infection.

3.3. Trial Patient Study

To further investigate the effect of PGF-Biopor®AB on scar healing, an empirical trial patient study using Vancouver Scar Scale parameters assessed scar-healing performance over one-month (Figure 11). After one month, firstly, regarding relief of surface irregularity, noticeable improvement in scar irregularity was observed with decreased irregularity, especially on the edges of the scar. On scar thickness, reduced hypertrophy was observed with thinning of the superficial scar. Regarding pliability for tissue elasticity, an observably smoother scar surface with overall improved scar elasticity was observed, changing from thicker elastic fibers to finer elastic fibers. Next, for pigmentation, a slightly reduced color was observed. Analyzing the literature data, SGS typically had efficacy upon being worn over the scar for 12–24 h per day for at least 2–3 months, and PGT had efficacy over 6 months [77,79]. Thus, the 1-month efficacy results for PGF-Biopor®AB confirmed efficacy optimization from PGT-SGS dual therapy and active-fluid transport. The improved hydration performance in WVTR and water uptake capability with sustainability further

supported adequate hydration and active-fluid transport, also supporting use of this treatment for scar healing.

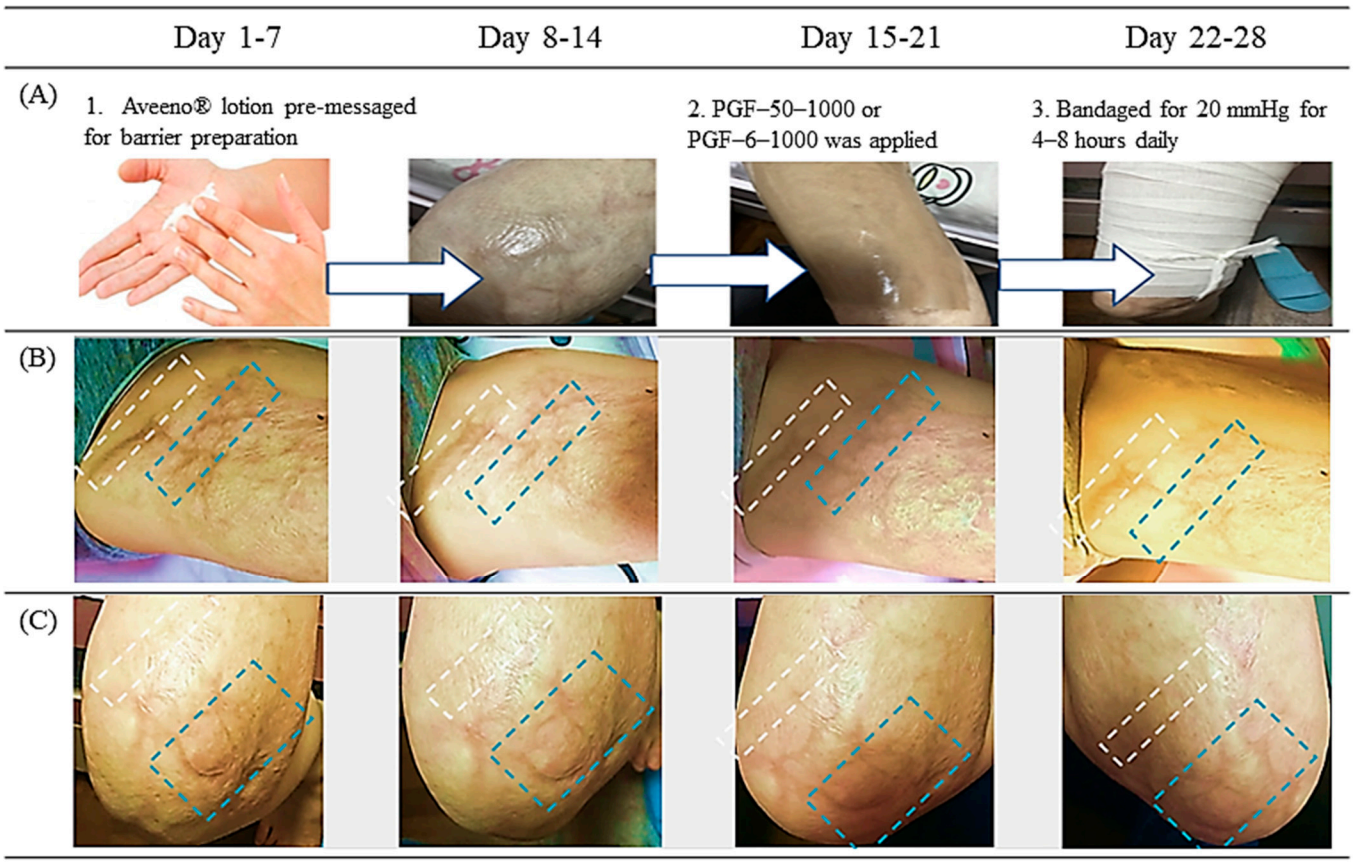

Figure 11. Trial patient study: ATDDS for PGF-Biopor®AB application on a burn patient (Carman Chong) with two zones of degree 2 and degree 3 scarring tissues from day 1-day 28, imaging every 7 days for treatment efficacy: (**A**). Healing processes of ATDDS, (**B**) Zone 1 (with PGF-50-1000), and (**C**) Zone 2 (with PGF-6-1000). Note: white for control without ATDDS application and blue with ATDDS application.

In the suggested ATDDS for PGF-Biopor®AB application, the drug layer containing Aveeno® functioned as an effective occlusive-diffusion-penetration for a source of water hydration in the first place. The continuous pressure-driven self-pumping activated warp insertion mobility for dynamic and sustainable diffusional transport of Aveeno® with water (the fluid) in the 3-D channel structure. The asymmetric "spiral-through-the-thickness" structure with channel and microchannels facilitated effective directional water transport. According to the seven elements of the Arzt heptahedron for skin hydration, the mechanical behavior of both a-keratin and b-keratin of skin depends highly on the degree of hydration [80,81]. Firstly, increasing hydration decreases scar tissue's stiffness and modulus because the keratin matrix absorbs moisture [81]. As a result, sufficient hydration should recover collagens tensile strength and elongation in scar tissue for earlier scar maturation [80]. Hence, Active-fluid transport strived for adequate hydration, and dual therapy enabled the reorganization of collagen and elastic fiber network. Therefore, the one-month efficacy results support the active silicone occlusive healing theory with PGT-SGS dual therapy and active-fluid transport.

4. Conclusions

This study developed a new self-pumping composite dressing of dual therapy and trauma-free active-fluid transport for improved hypertrophic scar healing. Results of comparative studies recorded improved hydration performance in water uptake and water permeability capabilities with sustainably enhanced one-month treatment efficacy in the empirical trial patient study. These results supported the PGF-Biopor®AB composite design, and PGT-SGS dual therapy achieved efficacy optimization and active-fluid transport with trauma-free dressing properties achieved ideal dressing performance. The "Biopor®AB-touching-skin" surfaces and warp insertion mobility realized tension shielding and pressure redistribution and yet eliminated the problems of either PGT or SGS performance alone for patient comfort. "Biopor®AB-touching-skin" surfaces demonstrated silicone therapy and trauma-free dressing performance. The active-fluid transport offered a WVTR of 233 $g/m^2/day$ with 4-day sustainability, which fulfilled the scar therapeutics' purpose of active hydration with water retention, for improved scar healing capability. The one-month efficacy optimization in degree-2 and degree-3 empirical trial patient studies is an encouraging result for a new direction in PGT-SGS dual therapy and active-fluid transport for scar therapeutics. The successful application of pre-strained screen printing for warp insertion mobility and the creation of a 3D channel structure for the active-fluid transport should offer new insights into the structural potential of pre-strained screen printing. Further studies may include in-hospital patient study, mathematical modeling for tensile and shear properties of the composite structure, and pressure redistribution performance of self-pumping PGT-SGS composite.

Author Contributions: K.-C.L.: Methodology, Validation, Formal analysis, Investigation, Writing—original draft. X.W., C.-W.K., N.N.: Methodology, Formal analysis, Writing—supervision, review, and editing. All authors have read and agreed to the published version of the manuscript.

Funding: This research was funded by [RGC GRF] grant number [A1600049].

Informed Consent Statement: Informed consent was obtained from all subjects involved in the study. Written informed consent has been obtained from the patient(s) to publish this paper.

Data Availability Statement: The authors confirm that the data supporting the findings of this study are available within the article.

Acknowledgments: The first author would like to thank SFT, The Hong Kong Polytechnic University, for PhD funding for a 4-year full-time research studentship. Our special thanks go to Ka Man Carman Chong, a patient, for patient study and review. Our special thanks go to Bin Fei and Akanksha Pragya for their contributions to the initial work. We would also like to acknowledge support from the Hong Kong Jockey Club Charities Trust.

Conflicts of Interest: Nothing to declare.

References

1. Gauglitz, G.G.; Korting, H.C.; Pavicic, T.; Ruzicka, T.; Jeschke, M.G. Hypertrophic scarring and keloids: Pathomechanisms and current and emerging treatment strategies. *Mol. Med.* **2011**, *17*, 113. [CrossRef] [PubMed]
2. *Reportlinker.com Announces the Release of the Report "Medical Aesthetics Market Product, End User—Global Forecast to 2025"*; Globe Newswire: New York, NY, USA, 2020.
3. Anthonissen, M.; Daly, D.; Janssens, T.; Van den Kerckhove, E. The effects of conservative treatments on burn scars: A systematic review. *Burns* **2016**, *42*, 508–518. [CrossRef]
4. Brown, M.B.; Martin, G.P.; Jones, S.A.; Akomeah, F.K. Dermal and transdermal drug delivery systems: Current and future prospects. *Drug Deliv.* **2006**, *13*, 175–187. [CrossRef]
5. Muir, I.F.K. On the nature of keloid and hypertrophic scars. *Br. J. Plast. Surg.* **1990**, *43*, 61–69. [CrossRef] [PubMed]
6. Mustoe, T.A. Evolution of silicone therapy and mechanism of action in scar management. *Aesthetic Plast. Surg.* **2008**, *32*, 82–92. [CrossRef] [PubMed]
7. Li, Y.; Zhu, C.; Fan, D.; Fu, R.; Ma, P.; Duan, Z.; Li, X.; Lei, H.; Chi, L. A bi-layer PVA/CMC/PEG hydrogel with gradually changing pore sizes for wound dressing. *Macromol. Biosci.* **2019**, *19*, 1800424. [CrossRef]
8. Monstrey, S.; Middelkoop, E.; Vranckx, J.J.; Bassetto, F.; Ziegler, U.E.; Meaume, S.; Téot, L. Updated scar management practical guidelines: Non-invasive and invasive measures. *J. Plast. Reconstr. Aesthetic Surg.* **2014**, *67*, 1017–1025. [CrossRef]

9. Ogawa, R. The most current algorithms for the treatment and prevention of hypertrophic scars and keloids: A 2020 update of the algorithms published 10 years ago. *Plast. Reconstr. Surg.* **2022**, *149*, 79. [CrossRef]
10. Wright, J.A.; Richards, T.; Srai, S.K.S. The role of iron in the skin and cutaneous wound healing. *Front Pharmacol. Front. Media S.A.* **2014**, *5*, 156. [CrossRef]
11. Kolarsick, P.A.J.; Kolarsick, M.A.; Goodwin, C. Anatomy and physiology of the skin. *J. Derm. Nurses Assoc.* **2011**, *3*, 203–213. [CrossRef]
12. Moore, A.; Marshall, C.; Longaker, M. Minimizing skin scarring through biomaterial design. *J. Funct. Biomater.* **2017**, *8*, 3. [CrossRef]
13. Tejiram, S.; Zhang, J.; Travis, T.E.; Carney, B.C.; Alkhalil, A.; Moffatt, L.T.; Shupp, J.W. Compression therapy affects collagen type balance in hypertrophic scar. *J. Surg. Res.* **2016**, *201*, 299–305. [CrossRef] [PubMed]
14. Mokos, Z.B.; Jović, A.; Grgurević, L.; Dumić-Čule, I.; Kostović, K.; Čeović, R.; Marinović, B. Current therapeutic approach to hypertrophic scars. *Front. Med.* **2017**, *4*, 83. [CrossRef] [PubMed]
15. Chow, L.; Yick, K.-L.; Kwan, M.-Y.; Yuen, C.-F.; Ng, S.-P.; Yu, A.; Yip, J. Customized fabrication approach for hypertrophic scar treatment: 3D printed fabric silicone composite. *Int. J. Bioprint.* **2020**, *6*, 262. [CrossRef] [PubMed]
16. Quinn, K.; Courtney, J.; Evans, J.; Gaylor, J.; Reid, W. Principles of burn dressings. *Biomaterials* **1985**, *6*, 369–377. [CrossRef] [PubMed]
17. Lalani, R.; Liu, L. Electrospun zwitterionic poly (sulfobetaine methacrylate) for nonadherent, superabsorbent, and antimicrobial wound dressing applications. *Biomacromolecules* **2012**, *13*, 1853–1863. [CrossRef]
18. Ye, S.; Jiang, L.; Wu, J.; Su, C.; Huang, C.; Liu, X.; Shao, W. Flexible amoxicillin-grafted bacterial cellulose sponges for wound dressing: In vitro and in vivo evaluation. *ACS Appl. Mater. Interfaces* **2018**, *10*, 5862–5870. [CrossRef]
19. Chiang, R.S.; Borovikova, A.A.; King, K.; Banyard, D.A.; Lalezari, S.; Toranto, J.D.; Widgerow, A.D. Current concepts related to hypertrophic scarring in burn injuries. *Wound Repair Regen.* **2016**, *24*, 466–477. [CrossRef]
20. Shen, J.; Xu, F.; Cheng, L.; Pan, W.; Ge, Y.; Li, J.; Zhang, J. Simulation of internal flow characteristics of an axial flow pump with variable tip clearance. *Water* **2022**, *14*, 1652. [CrossRef]
21. Ji, H.; Wei, M.; Liu, R.; Chang, C. Drive Control Simulation and Experimental Studies on the Flow Characteristics of a Pump Injector. *IEEE Access* **2020**, *8*, 35672–35681. [CrossRef]
22. Young, D.F.; Tsai, F.Y. Flow characteristics in models of arterial stenoses—I. Steady flow. *J. Biomech.* **1973**, *6*, 395–410. [CrossRef] [PubMed]
23. Chang, H.; Hong, S.; Yu, D.; Peng, G.; Du, J.; Yuan, S. Flow Characteristic Analysis of the Self-Priming Pump Based on the Population Balance Model. *Front. Energy Res.* **2022**, *10*, 404. [CrossRef]
24. Akbarzadeh, P. Numerical study of thermohydrodynamic characteristics of oil tilting-pad journal bearings with a self-pumping fluid flow circulation. *Tribol. Trans.* **2015**, *58*, 18–30. [CrossRef]
25. Sidgwick, G.P.; McGeorge, D.; Bayat, A. A comprehensive evidence-based review on the role of topicals and dressings in the management of skin scarring. *Arch. Dermatol. Res.* **2015**, *307*, 461–477. [CrossRef]
26. Klare, M.; Frank, G.; Markus, K.; Veit, T. Elastomer Materials. Germany Patent DE 10 2011 115 061, 11 April 2013.
27. Verdier-Sévrain, S.; Bonté, F. Skin hydration: A review on its molecular mechanisms. *J. Cosmet. Dermatol.* **2007**, *6*, 75–82. [CrossRef] [PubMed]
28. Xu, B.; Li, A.; Wang, R.; Zhang, J.; Ding, Y.; Pan, D.; Shen, Z. Elastic Janus film for wound dressings: Unidirectional biofluid transport and effectively promoting wound healing. *Adv. Funct. Mater.* **2021**, *31*, 2105265. [CrossRef]
29. Zhang, Y.; Tian, M.; Wang, L.; Zhao, H.; Qu, L. Flexible Janus textile-based electroosmotic pump for large-area unidirectional positive water transport. *Adv. Mater. Interfaces* **2020**, *7*, 1902133. [CrossRef]
30. Zhou, L.; Xu, P.; Dong, P.; Ou, X.; Du, X.; Chen, Y.; Zhang, X.; Gao, W.; Gao, G. A self-pumping dressing with in situ modification of non-woven fabric for promoting diabetic wound healing. *Chem. Eng. J.* **2023**, *457*, 141108. [CrossRef]
31. Shao, Z.; Chen, J.; Ke, L.-J.; Wang, Q.; Wang, X.; Li, W.; Zheng, G. Directional transportation in a self-pumping dressing based on a melt electrospinning hydrophobic mesh. *ACS Biomater. Sci. Eng.* **2021**, *7*, 5918–5926. [CrossRef]
32. Qi, L.; Ou, K.; Hou, Y.; Yuan, P.; Yu, W.; Li, X.; Wang, B.; He, J.; Cui, S.; Chen, X. Unidirectional water-transport antibacterial trilayered nanofiber-based wound dressings induced by hydrophilic-hydrophobic gradient and self-pumping effects. *Mater. Des.* **2021**, *201*, 109461. [CrossRef]
33. Si, Y.; Chen, L.; Yang, F.; Guo, F.; Guo, Z. Stable Janus superhydrophilic/hydrophobic nickel foam for directional water transport. *J. Colloid Interface Sci.* **2018**, *509*, 346–352. [CrossRef]
34. Zhu, H.; Zhi, C.; Meng, J.; Wang, Y.; Liu, Y.; Wei, L.; Fu, S.; Miao, M.; Yu, L. A self-pumping dressing with multiple liquid transport channels for wound microclimate management. *Macromol. Biosci.* **2022**, *23*, 2200356. [CrossRef] [PubMed]
35. Du, W.; Zhang, Z.; Fan, W.; Gao, W.; Su, H.; Li, Z. Fabrication and evaluation of polydimethylsiloxane modified gelatin/silicone rubber asymmetric bilayer membrane with porous structure. *Mater. Des.* **2018**, *158*, 28–38. [CrossRef]
36. Gencer, Z.A.; Odabas, S.; Sasmazel, H.T.; Piskin, E. Microporous silicone biomaterials with modified surface chemistry: Production and characterization. *J. Bioact. Compat. Polym.* **2012**, *27*, 419–428. [CrossRef]
37. Magniez, K.; Zaidi, B.M.; Zhang, J.; Miao, M. Prestrained twistless flax yarn as reinforcement for polymer-matrix composites. *Polym. Compos.* **2020**, *41*, 930–938. [CrossRef]
38. Jaffe, M.; Hammond, W.; Tolias, P.; Arinzeh, T. (Eds.) *Characterization of Biomaterials*; Elsevier: Amsterdam, The Netherlands, 2012.

39. Gu, R.; Ngan, A.H.W. Effects of pre-straining and coating on plastic deformation of aluminium micropillars. *Acta Mater.* **2012**, *60*, 6102–6111. [CrossRef]
40. Ly, N.G.; Denby, E.F. A CSIRO inter-laboratory trial of the KES-F for measuring fabric properties. *J. Text. Inst.* **1988**, *79*, 198–219. [CrossRef]
41. McNeely, M.R.; Sputea, M.K.; Tusneem, N.A.; Oliphant, A.R. Sample processing with hydrophobic microfluidics. *J. Assoc. Lab. Autom.* **1999**, *4*, 30–33. [CrossRef]
42. Hong, S.; Minary-Jolandan, M.; Naraghi, M. Controlling the wettability and adhesion of carbon fibers with polymer interfaces via grafted nanofibers. *Compos. Sci. Technol.* **2015**, *117*, 130–138. [CrossRef]
43. Andersson, C.-H.; Dartman, T.; Gredinger, P.; Asplund, J.; Strandqvist, H. Flexible composites, strength, deformation, and fracture processes. 1. reinforcement structures and tensile strength. *Mech. Compos. Mater.* **1998**, *34*, 525–536. [CrossRef]
44. Schüth, F.; Sing, K.S.W.; Weitkamp, J. *Handbook of Porous Solids*; Wiley: Hoboken, NJ, USA, 2002.
45. Wang, L.; Felder, M.; Cai, Y. Study of properties of medical compression garments fabrics. *J. Fiber Bioeng. Inform.* **2011**, *4*, 15–22. [CrossRef]
46. Choi, F.K. Modeling of Singles and Two-Ply Staple Fiber Yarns. Ph.D. Thesis, Institute of Textiles and Clothing of the Hong Kong Polytechnic University, Department of Applied Mathematics, Hong Kong Polytechnic University, Hong Kong, China, 1997.
47. Choi, F.K. Mechanical properties of wrapped yarn. *Text. Asia* **1991**, *4*, 33–37.
48. Crookston, J.J.; Long, A.C.; Jones, I.A. A summary review of mechanical properties prediction methods for textile reinforced polymer composites. Proceedings of the Institution of Mechanical Engineers, Part L. *J. Mater. Des. Appl.* **2005**, *219*, 91–109.
49. Wu, W.L.; Hamada, H.; Kotaki, M.; Maekawa, Z. Design of knitted fabric reinforced composites. *J. Reinf. Plast. Compos.* **1995**, *14*, 786–798. [CrossRef]
50. Nasser, J.; Lin, J.; Steinke, K.; Sodano, H.A. Enhanced interfacial strength of aramid fiber reinforced composites through adsorbed aramid nanofiber coatings. *Compos. Sci. Technol.* **2019**, *174*, 125–133. [CrossRef]
51. McCoy, R.J.; Jungreuthmayer, C.; O'Brien, F.J. Influence of flow rate and scaffold pore size on cell behaviour during mechanical stimulation in a flow perfusion bioreactor. *Biotechnol. Bioeng.* **2012**, *109*, 1583–1594. [CrossRef] [PubMed]
52. Song, Y.; Lei, M.; Lei, J.; Li, Z. A scalable hybrid fiber and its textile with pore and wrinkle structures for passive personal cooling. *Adv. Mater. Technol.* **2020**, *5*, 2000287. [CrossRef]
53. Dai, N.-T.; Williamson, M.; Khammo, N.; Adams, E.; Coombes, A. Composite cell support membranes based on collagen and polycaprolactone for tissue engineering of skin. *Biomaterials* **2004**, *25*, 4263–4271. [CrossRef] [PubMed]
54. Xu, R.; Luo, G.; Xia, H.; He, W.; Zhao, J.; Liu, B.; Tan, J.; Zhou, J.; Liu, D.; Wang, Y.; et al. Novel bilayer wound dressing composed of silicone rubber with particular micropores enhanced wound re-epithelialization and contraction. *Biomaterials* **2015**, *40*, 1–11. [CrossRef]
55. Zeng, W.; Shu, L.; Li, Q.; Chen, S.; Wang, F.; Tao, X.M. Fiber-based wearable electronics: A review of materials, fabrication, devices, and applications. *Adv. Mater.* **2014**, *26*, 5310–5336. [CrossRef]
56. Jang, B.Z. Control of interfacial adhesion in continuous carbon and Kevlar fiber reinforced polymer composites. *Compos. Sci. Technol.* **1992**, *44*, 333–349. [CrossRef]
57. Comyn, J. What are adhesives and sealants and how do they work? In *Adhesive Bonding*; Woodhead Publishing: Cambridge, UK, 2021; pp. 41–78.
58. Wang, H.; Ding, J.; Dai, L.; Wang, X.; Lin, T. Directional water-transfer through fabrics induced by asymmetric wettability. *J. Mater. Chem.* **2010**, *20*, 7938–7940. [CrossRef]
59. Wang, H.; Wang, X.; Lin, T. Unidirectional water transfer effect from fabrics having a superhydrophobic-to-hydrophilic gradient. *J. Nanosci. Nanotechnol.* **2013**, *13*, 839–842. [CrossRef] [PubMed]
60. Sun, F.; Chen, Z.; Zhu, L.; Du, Z.; Wang, X.; Naebe, M. Directional trans-planar and different in-plane water transfer properties of composite structured bifacial fabrics modified by a facile three-step plasma treatment. *Coatings* **2017**, *7*, 132. [CrossRef]
61. Jin, M.; Chen, W.; Li, Z.; Zhang, Y.; Zhang, M.; Chen, S. Patterned bacterial cellulose wound dressing for hypertrophic scar inhibition behavior. *Cellulose* **2018**, *25*, 6705–6717. [CrossRef]
62. Hu, G.; Kang, J.; Ng, L.W.T.; Zhu, X.; Howe, R.C.T.; Jones, C.G.; Hersam, M.C.; Hasan, T. Functional inks and printing of two-dimensional materials. *Chem. Soc. Rev.* **2018**, *47*, 3265–3300. [CrossRef]
63. Zheng, S.; Jiang, Y.; Wu, X.; Xu, Z.; Liu, Z.; Yang, W.; Yang, M. Highly sensitive pressure sensor with broad linearity via constructing a hollow structure in polyaniline/polydimethylsiloxane composite. *Compos. Sci. Technol.* **2021**, *201*, 108546. [CrossRef]
64. Ji, J.; Ge, X.; Pang, X.; Liu, R.; Wen, S.; Sun, J.; Liang, W.; Ge, J.; Chen, X. Synthesis and characterization of room temperature vulcanized silicone rubber using methoxyl-capped MQ silicone resin as self-reinforced cross-linker. *Polymers* **2019**, *11*, 1142. [CrossRef]
65. Zou, C.; Lao, L.; Chen, Q.; Fan, J.; Shou, D. Nature-inspired moisture management fabric for unidirectional liquid transport and surface repellence and resistance. *Energy Build.* **2021**, *248*, 111203. [CrossRef]
66. O'connor, S.M.; Hanson, I.B.; Bente IV, P.F.; Clemente, M.J. Fluid Restriction Mechanisms for Drug Delivery Pumps. U.S. Patent No. 10,617,820, 14 April 2020.
67. Comanns, P. Passive water collection with the integument: Mechanisms and their biomimetic potential. *J. Exp. Biol.* **2018**, *221*, jeb153130. [CrossRef]

68. Hollies, N.R.; Kaessinger, M.M.; Watson, B.S.; Bogaty, H. Water transport mechanisms in textile materials: Part II: Capillary-type penetration in yarns and fabrics. *Text. Res. J.* **1957**, *27*, 8–13. [CrossRef]
69. Gupta, M.; Singh, R. PLA-coated sisal fibre-reinforced polyester composite: Water absorption, static and dynamic mechanical properties. *J. Compos. Mater.* **2019**, *53*, 65–72. [CrossRef]
70. Hollies, N.R.S.; Kaessinger, M.M.; Bogaty, H. Water transport mechanisms in textile materials1 Part I: The role of yarn roughness in capillary-type penetration. *Text. Res. J.* **1956**, *26*, 829–835. [CrossRef]
71. Jhanji, Y.; Gupta, D.; Kothari, V.K. Liquid transfer properties and drying behavior of plated knitted fabrics with varying fibre types. *Indian J. Fibre Text. Res.* **2015**, *40*, 162–169.
72. Abdul-Bari, M.M.; McQueen, R.H.; Nguyen, H.; Wismer, W.V.; de la Mata, A.P.; Harynuk, J.J. Synthetic clothing and the problem with odor: Comparison of nylon and polyester fabrics. *Cloth. Text. Res. J.* **2018**, *36*, 251–266. [CrossRef]
73. Sweeney, I.R.; Miraftab, M.; Collyer, G. Absorbent alginate fibres modified with hydrolysed chitosan for wound care dressings–II. pilot scale development. *Carbohydr. Polym.* **2014**, *102*, 920–927. [CrossRef]
74. Lou, C.W.; Lin, C.W.; Chen, Y.S.; Yao, C.H.; Lin, Z.S.; Chao, C.Y.; Lin, J.H. Properties evaluation of Tencel/cotton nonwoven fabric coated with chitosan for wound dressing. *Text. Res. J.* **2008**, *78*, 248–253. [CrossRef]
75. Lamke, L.-O.; Nilsson, G.; Reithner, H. The evaporative water loss from burns and the water-vapour permeability of grafts and artificial membranes used in the treatment of burns. *Burns* **1977**, *3*, 159–165. [CrossRef]
76. Liu, X.; Liu, Y.; Du, J.; Li, X.; Yu, J.; Ding, B. Breathable, stretchable, and adhesive nanofibrous hydrogels as wound dressing materials. *Eng. Regen.* **2021**, *2*, 63–69. [CrossRef]
77. Berman, B.; Perez, O.A.; Konda, S.; Kohut, B.E.; Viera, M.H.; Delgado, S.; Li, Q. A review of the biological effects, clinical efficacy, and safety of silicone elastomer sheeting for hypertrophic and keloid scar treatment and management. *Dermatol. Surg.* **2007**, *33*, 1291–1303.
78. Kannon, G.A.; Garrett, A.B. Moist wound healing with occlusive dressings: A clinical review. *Dermatol. Surg.* **1995**, *21*, 583–590. [CrossRef] [PubMed]
79. Tran, B.; Wu, J.J.; Ratner, D.; Han, G. Topical scar treatment products for wounds: A systematic review. *Dermatol. Surg.* **2020**, *46*, 1564–1571. [CrossRef] [PubMed]
80. Meyers, M.A.; Chen, P.Y. *Biological Materials Science: Biological Materials, Bioinspired Materials, and Biomaterials*; Cambridge University Press: Cambridge, UK, 2014.
81. Meyers, M.A.; Chen, P.Y.; Lin, A.Y.M.; Seki, Y. Biological materials: Structure and mechanical properties. *Prog. Mater. Sci.* **2008**, *53*, 1–206. [CrossRef]

Disclaimer/Publisher's Note: The statements, opinions and data contained in all publications are solely those of the individual author(s) and contributor(s) and not of MDPI and/or the editor(s). MDPI and/or the editor(s) disclaim responsibility for any injury to people or property resulting from any ideas, methods, instructions or products referred to in the content.